Spatiotemporal patterns of limnological parameters on the Amazon floodplain

Cláudio Clemente Faria Barbosa, Evlyn Márcia Leão de Moraes Novo

Coordenação de Observação da Terra, Instituto Nacional de Pesquisas Espaciais, São José dos Campos, Avenida dos Astronautas, 1758, CEP 12 201 970, Brasil.

+55 12 3945 6480

+55 12 3945 6468

cláudio@dpi.inpe.br

www.dpi.inpe.br/~claudio

John M. Melack

Bren School of Environmental Science and Management, University of California, Santa Barbara, CA 93106, USA

Mary Gastil-Buhl

Institute for Computational Earth System Science, University of California, Santa Barbara, CA 93106, USA,

Waterloo Pereira Filho

Departamento de Geografia, Universidade Federal de Santa Maria, Faixa de Camobi, km 9, Campus Universitário, Santa Maria, CEP 97105-900, Rio Grande do Sul, Brasil

Total text pages: 30

Tables: 4

Figures: 8

Abstract

We applied spatial data analysis and geostatistical procedures to a limnological dataset gathered on the Amazon floodplain. Variographic analysis and ordinary kriging interpolation were used to identify and describe spatiotemporal patterns of variability in limnological parameters that are relevant to understand the dynamics of water circulation on the floodplain. In spite of the complexity of the processes underlying the spatiotemporal patterns, this approach demonstrated that the heterogeneity in the seasonal water composition is forced not only by the flood pulse but also by topography and wind.

Keywords: Amazon floodplain lakes, spatiotemporal patterns of limnological parameters, ordinary kriging, remote sensing, spatial modeling

Introduction

The area covered by the mainstem Amazon floodplain in Brazil is approximately 100000 km^2 (Hamilton et al. 2002). Floodplain ecosystem function is influenced by the chemical composition and hydrology of the inflows to the system. The physical-chemical properties of waters within the Amazon basin vary widely as a function of water sources, soil type, vegetation cover and climatic conditions. Hence, mapping the spatial patterns of flooding is important to understanding these floodable ecosystems. The dimensions and complexity of Amazon water bodies makes remote sensing a feasible approach to understanding the regional dynamics of water circulation on Amazon floodplains. Studies have demonstrated that optical images can be used to trace routing of water on floodplains (Mertes et al., 1993). Suspended sediments can be a natural tracer (Mobley, 1994) for detecting spatial dynamics of inflows and phytoplankton distributions can provide complementary information (Costa, 1992; Novo et al, 2006).

While data gathered by remote sensing are usually modeled as a regular grid of cells, sampling at ground level is usually irregular and sparse. Transforming these irregular samples into a regular grid, inferring values for unsampled locations, produces a more complete description of the spatial variability.

Several interpolation methods are available and can be used to generate regular grids from irregularly sampled data (Burrough and McDonnell, 1998; Felgueiras, 1995; Bonham-Carter, 1994). When data are abundant, most of the interpolation techniques give similar results. However, when data are sparse, the choice of the interpolation method is crucial to avoiding misleading results (Burrough and McDonnell, 1998). The problems occur because these methods consider only the distance among samples and unvisited points, not taking into account the differential weight of each sample over its region of influence, and they do not consider that the region of influence may be anisotropic, with different spatial correlation among samples in distinct directions. Geostatistical procedures that consider anisotropic regions of influence, during spatial interpolation, have been developed (Burrough and McDonnell, 1998; Isaaks and Srivastava, 1989). The procedures, called spatial modeling, offer a way to identify, describe and account for the anisotropic spatial continuity during inference of values at unsampled locations. The purpose of this paper is to take advantage of geospatial techniques to describe and identify patterns of spatiotemporal variability of water constituents in order to improve the understanding of water exchange between the Amazon River and its floodplain. The Amazon River and the Curuai floodplain were selected and approached as a dynamic system. Data were collected in different states of the system and submitted to variographic analysis and ordinary kriging interpolation.

Spatial modeling concepts

The behavior of spatial phenomena is often the result of a mixture of first and second order effects (Matheron, 1971). The first order effects are related to the variation in the mean value of the process in space; they are considered global or large scale. Second order effects result from the structure of spatial correlation or spatial dependence; they are local or small scale effects and represent the tendency for deviation in values of the

3

process from its mean value to "follow" each other in neighboring sites (Bailey, 1995). Because of this mixture of effects, spatial variations of continuous attributes are often too irregular to be modeled by a simple, smooth mathematical function (Isaaks and Srivastava, 1989). Regionalized variable theory assumes that the spatial variation of any variable can be expressed (Equation 1) as the sum of three components (Matheron, 1971): (a) a structural component, having a constant mean or trend (first order effect or deterministic component); (b) a random, but spatially correlated component (second order effect or stochastic component); and (c) a spatially uncorrelated random noise or residual error component. The large-scale variation is modeled by a deterministic function and small-scale variation by a stochastic process.

If x is a spatial position, the value of a continuous attribute at x position, based on regionalized variable theory, is given by a random function Z(x):

$$Z(x) = m(x) + \varepsilon'(x) + \varepsilon''$$ (1)

Where m (x) is a deterministic function describing the first order effect; ε' (x) is the random component, which holds the information of spatial correlation; and ε'' is a spatially independent Gaussian noise component.

The kriging inference concentrates on modeling the component that holds the information of spatial correlation $\varepsilon'(x)$, and includes it in the interpolation process, in order to refine the inferences. Several concepts and statistical tools are used:

Continuity or *spatial autocorrelation* is an intrinsic feature of spatial data, which is characterized by similarity among values of an attribute in its neighborhood. However, an environmental dataset seldom shows uniform spatial continuity in different directions, and instead has *anisotropic* behavior. In general, some physical feature inherent in the studied phenomenon controls the orientation of the anisotropy (Isaaks and Srivastava, 1989).

4

To describe how spatial continuity changes as function of distance and direction, statistical tools such as autocorrelation and autocovariance functions or a variogram may be used (Burrough and McDonnell, 1998; Dale et al. 2002) but, a variogram is the most traditional choice (Isaaks and Srivastava, 1989). While the autocorrelation and autocovariance functions deal with the similarity coefficient, a variogram uses the dissimilarity coefficient (Goovaerts, 1997). The interpretation of spatial continuity based on a variogram must be done taking into account that the smaller the variogram value, the higher the spatial continuity, while a high value represents a lower spatial continuity (Gringarten and Deutsch, 2001).

Some parameters are used to describe important features of a variogram. As the separation distance between pairs of samples increases, the corresponding variogram value also increases. When an increase in the separation distance no longer causes a corresponding increase in the variogram value, it reaches a plateau. The average distance at which the variogram reaches this plateau is called the *range*. Within this distance samples remain spatially correlated, and at distances greater than the *range*, one assumes that there is no spatial dependence or spatial correlation between samples. The variogram value at range distance is called the *sill*. The value of the *sill* is usually equivalent to the traditional sample variance. A longer range in a given direction means that the variable has more continuity in that direction. This longer range or maximum continuity direction is called the anisotropy direction.

A mathematic model describing the spatial variability of a dataset is obtained fitting an empirical variogram to a mathematic function. Inference to unsampled locations can then be obtained from this fitted variogram. The functions most used to fit variograms are spherical, exponential, and Gaussian. The choice of the function usually depends on the shape of the empirical variogram near the origin. If the phenomenon is more spatially continuous, as measured by its major autocorrelation among sampling values,

then the empirical variogram will have a parabolic behavior near the origin; in such cases, the Gaussian function will usually provide the best fit. If the empirical variogram has a linear behavior near the origin, indicating minor spatial continuity, either the spherical or the exponential function is preferable. The variogram shape can be revealing about the kind of spatial variation present on the variable under investigation. An empirical variogram fitted to an exponential function suggests a dataset with a spatial pattern characterized by gradual transition among several patterns interfering with each other. A variogram fitted to a Gaussian function, indicates a smoothly varying pattern, and one fitted to a spherical function, indicates that one pattern is dominant (Burrough and McDonnell, 1998).

Several kriging techniques are available. This paper, whose objective is to identify spatiotemporal patterns in water bodies, focuses on ordinary kriging, which is a direct generalization of the simple kriging and in practical terms, easier to apply (Bailey, 1995). As the primary focus of ordinary kriging is prediction, the components of Equation 1 are simultaneously and implicitly estimated as part of the prediction process and are not visible in the results.

Methods

Study area

The Lago Grande de Curuai (LGC) floodplain, located along the Amazon River near Obidos and 900 km upstream from the Atlantic Ocean, is a complex system of about 30 shallow, interconnected lakes linked to the Amazon River by several channels and including open water, flooded savannas and floating grasses (Martinez and Le Toan. 2007; Fig. 1-a). Maurice Bourgoin et al. (2007) examined fluvial transport and storage of sediments within the Curuaí floodplain. Their analyses were derived from hydrological data, a monitoring network operated between 1999 and 2003, and from

total suspended solids concentrations acquired near Óbidos (Guyot et al. 2005), multi-temporal remote sensing images and radar altimetry data, and the hydrological model of Bonnet et al. (in press).

The dynamics of flooding are related to Amazon River stage fluctuations and have an annual monomodal pattern (Junk et al., 1989) (Fig. 1-b) that can be characterized by four periods: 1) In January and February water levels rise at rates of over 3.6 cm d^{-1}. 2) In April, May and June water levels rise at rates less than 1.2 cm d^{-1} 3). In August, September and October water levels fall at rates over 3.6 cm d^{-1}. 4) In October and November water levels are low and changing little. During the rising water stage, Amazon River water flows into the floodplain enlarging open water flooded area from 700 km^2 (Fig. 1-c) to 1600 km^2 (Fig. 1-d) (Barbosa, 2005).

The seasonal range in level from 1993 to 2002 (maximum minus minimum) varied from 500 cm to 700 cm, and the range of interannual amplitude was as large as 160 cm (Table 1).

[insert Figure 1 about here]

[insert table 1 about here]

Field sampling and measurements

Based on examination of the annual hydrograph (Fig. 1-b), four *states* were selected and sampled to describe the dynamics of system (Fig. 2; Table 2). *States 2* and *4* are characterized by minimum rates of change in the water level (stable states) and *states 1* and *3* by maximum rates of change representing transitions states.

[insert Figure 2 about here]

[insert table 2 about here]

The distribution of sampling stations was based on maps of water masses (Fig. 3) derived from unsupervised classification of Landsat TM images (Bins et al., 1996;

Barbosa et al., 2000) representative of each state. Details of this methodological approach and field campaigns are described in Barbosa (2004).

[insert Figure 3 about here]

Water samples for laboratory analysis were collected from approximately 70 points, and in situ measurements were done concurrently at approximately 200 points on each field campaign. This paper focuses on total suspended sediment (TSS) and chlorophyll because of their importance for the understanding the dynamics of the Amazon River-floodplain system using remote sensing (Curran and Novo, 1988; Novo et al. 1989; Goodin et al. 1993; Mobley, 1994; Allee and Johnson, 1999). In addition, pH was included based on in situ measurements only.

The pH was measured at surface and at the Secchi depth, using a Horiba water quality instrument(model U-10). The instrument was calibrated every morning (Horiba, 1991). The water samples were collected by integrating the water column from surface to the Secchi depth. The samples were kept at cool temperature and filtered the same day. TSS was determined based on Wetzel and Likens (1991) and chlorophyll analyses were based on Nush (1980).

To increase the number of stations with TSS data, a regression model was built using paired measurements of turbidity and TSS (Fig. 4). Details are fully described in Barbosa (2005).

[insert Figure 4 about here]

Results

Within and between seasonal stages pH, turbidity, and TSS and chlorophyll concentrations varied considerably (Table 3). Among all the stages TSS ranged from a

minimum of 5.5 mg/l to a maximum of 1138 mg/l, and chlorophyll ranged from a

minimum of 0.2 μg/l to a maximum of 350 μg/l.

[insert table 3 about here]

To identify large-scale spatial trends an analysis for tendency was performed. Each

parameter was clustered into six ranked groups, above and below its mean value with

the range for clustering defined in terms of standard deviation units (Fig. 5-a).

Northern-southern and eastern-western tendency analysis using Lowess (*locally*

weighted regression scatter plot smoothing) revealed, for example, an increase in the

eastern-western direction in TSS concentration (Fig. 5-b). The results from these

analyses, applied over all selected parameters, were then used in the variographic

analysis

[insert Figure 5 about here]

A surface variographic analysis was used to detect axes of anisotropy, and indicated that

all parameters have a similar direction of anisotropy, approximately 97^0 with respect to

north (Fig. 6-a, Table 4). This direction, defined by the longer axis of the ellipse that

surrounds the surface variogram, identifies the direction of the highest spatial

autocorrelation. For LGC, the anisotropy directions were related to the predominant

direction of water flow. Barbosa (2005), using high resolution bathymetry, mapped a

major channel in LGC and inferred that the seasonal winds and the channel were two of

the main parameters controlling the direction of flow on the floodplain.

Directions around the anisotropy axes were explored and empirical variograms were

built and fitted to mathematical models. The parameters extracted from the fitted

variogram, summarized in Table 4, were used for ordinary kriging interpolation, using

SPRING (Camara et al., 1996), (www.dpi.inpe.br/spring).

[insert Figure 6 about here]

[insert table 4 about here]

9

Fig. 7 shows in shades of gray the results of ordinary kriging interpolation applied to pH, TSS and chlorophyll. These images provide a refined description of the spatiotemporal variability of these parameters.

[insert Figure 7 about here]

Discussion

The mean concentrations of TSS changed from 14.5 in state 2 to 463 mg/l in state 4. The floodplain had lower TSS concentration than the Amazon River during the states 1 and 2, and higher values during the states 3 and 4 (Table 3). These spatiotemporal dynamics of concentration and spatial distribution of TSS were likely driven by differences in wind, water depth, and movements of water. Weekly wind mean speed increased from 2.6 to 4.5 m/s from early September to the end of December 2004 (Fig. 8-b). In this period, there was no significant water input from the Amazon River since the water level was falling. Mean depth was less than 1 m during state 4, and resuspension was the likely cause for the high TSS concentrations. (Table 3).

The northern area closer to the Amazon River had higher TSS concentration than the mean floodplain values during states 3 and 4. Part of this area remains terrestrial during state 4 (Fig. 1-c), indicating that low depth during state 3 facilitated sediment resuspension.

[insert Figure 8 about here]

State 4, the lowest water level, occurred on November 8, 2003, and by November 9 water levels were rising. Field measurements were collected from November 22 to December 2 (Table 2), and on December 2, the gauging station on LGC floodplain registered water level 20 cm higher than November 8. From the beginning of rising water up to a level 700 cm higher, the inflows from the mainstream into the floodplain occurred mainly through the two perennial, approximately 100 meters wide channels,

10

located in the south-eastern extremity of the LGC floodplain (Barbosa, 2006; Maurice Bourgoin et al. 2007, Bonnet et al. in press,). Once on the floodplain, the water spreads, with a predominant flow in a western direction constrained by topography (Barbosa, 2006). The mixture of this inflow with mean TSS concentration of 60 mg/l (Table 3) with the water residing on the floodplain, with mean TSS concentration of 463 mg/l, caused a significant directional gradient, revealed by eastern-western Lowess (Fig. 5-b or dark shades in Fig. 7-column B). After this transitional period (from state 4 to state 1), the state 1 conditions were established, with a larger amount of riverine input, the mean TSS increased from 60 to 161 mg/l in the river water and decreased from 462 to 98 mg/l in the floodplain water. As the year progressed the Amazon River's contribution to the floodplain from the western-northern border increased, as the water reached the lakes through several narrow channels as seen as white shades on figure 7b-state 1.

Upon reaching the floodplain, the water speed decreased and deposition was responsible for reducing the TSS concentration. The TSS clustering map for state 1 revealed that 60% of TSS samples had concentrations between 45 and 98 mg/l. These sample points represented more than 50% of the floodplain area.

 The empirical variograms for states 2 and 3 were fitted to an exponential function (Table 4), with an anisotropy angle of 96^0 and 105^0, respectively. An exponential variogram suggests a dataset with a spatial pattern characterized by gradual transition among several patterns interfering with each other (Burrough, 1998). The variogram for state 4 was fitted to a Gaussian function, indicating a smoothly varying pattern for TSS, which is visible in Fig. 7-b. The state 1 dataset was fitted to a spherical function, indicating that one pattern is dominant for TSS. This is in accordance with the TSS clustering map for state 1, which revealed that 60% of TSS samples had concentration between mean value and minus one standard deviation below.

The degree of homogeneity or spatial autocorrelation of TSS, described by the range parameter (Table 4), is larger for state 1 (39440 meters), smaller in state 3 (5700 meters) and similar in states 2 and 4. States 3 and 4, with anisotropy factors of 1 (zonal anisotropy) and 0.77, respectively, have nearly isotropic homogeneity, and states 1 and 2 with anisotropy factors of 0.43 and 0.44, respectively, have directional homogeneity. In tropical lakes, such as LGC, the temperature is not likely limiting phytoplankton growth and does not have significant effects on its spatial and temporal distribution. In these lakes the availability of nutrients and underwater radiation are the main factors that control the phytoplankton spatial distribution (Esteves, 1998). Chlorophyll, an indicator of phytoplankton abundance, had values varying from 8.3 µg/l during state 1 to a maximum of 68.8 µg/l during state 3 (Table 3). The increase of chlorophyll concentration from state 1 to 2 and from state 2 to 3, was related to the increase of nutrients and changes in underwater radiation because nutrients reach the floodplain as sediment-laden water from Amazon River. The water speed reduced on the floodplain, favoring sediment deposition, and as consequence increasing underwater radiation, confirmed by mean Secchi depths of: state 1= 0.11 m, state 2 = 0.58 m; state 2 = 0.22 m; state 3 = 0.07 m. The maximum Secchi depths were 0.2 m, 1.2 m, 0.77 m and 0.35 m, respectively.

The chlorophyll had a heterogeneous spatiotemporal distribution, with well-defined "patches" or clusters of greater concentration (white shades in Fig. 7-column C). All empirical variograms for chlorophyll were fitted to Gaussian models (Table 7) with anisotropy angle of 106^0 in state 4 and 96^0 in the others. According to Burrough, (1998), a spatial dataset fitted to Gaussian models indicates a smoothly varying pattern. The largest spatial homogeneity for chlorophyll (Table 4) occurs in state 3, which is the state with the smallest TSS homogeneity. In this state the chlorophyll homogeneity is 38% larger than that of TSS.

12

The pH in the Amazon River was nearly constant (~6.5) while on the floodplain it increased, in mean, from 6.7 during the state 4 to 7.7 at the state 3 (Table 3). Minimum values of pH, between 4.7 and 5.2, were found at state 4 in clear water streams flowing from "terra firme" forest that reach the floodplain, and maximum values, between 9 and 9.4, were found at states 1 and 3, in floodplain areas with algal blooms. The pH showed spatial heterogeneity at states 2 and 3, mainly close to borders, displaying "patches" of low pH values (Fig. 7-A). The pH datasets for states 3 and 4 were fitted to a Gaussian model, suggesting a smoothly varying pattern, while for states 1 and 2 it was fitted to a spherical model, suggesting one dominant pattern. Based on the variogram range parameter, pH showed larger spatial homogeneity than TSS and chlorophyll in all states of the system.

Conclusions

The results revealed that, in spite of considerable complexity, the analyses generated information of high explanatory value regarding the patterns of spatial variability on the floodplain. The thematic clustered maps and directional Lowess aided understanding of the spatial context of the dataset and supplied information to model the structure of spatial variability. The variographic analysis proved to be an effective way to analyze spatial dynamics of environmental processes.

The surface variograms indicated the directions of anisotropy, reducing iterative analysis to built directional variograms. The construction and fitting of variograms to mathematical functions, was an effective procedure to analyze the spatial behavior of the parameters under study. The results of ordinary kriging interpolation and their representation as a gray scale images proved appropriate as a form to provide an overview of parameters' behavior and to identify spatial patterns.

The results showed heterogeneous spatiotemporal variability in the water composition on the LGC floodplain, and patterns revealed that the dynamics were forced not only by the flood pulse but also by the topography and wind. The flood pulse, however, by controlling the water level in the floodplain, creates the baseline set upon which the other forcing functions act.

The results also corroborate the importance of remote sensing techniques in helping the allocation of sampling sites due to the large spatial and temporal variability of the limnological variables.

Acknowledgements

References

Allee RJ, Johnson JE (1999) Use of satellite imagery to estimate surface chlorophyll a and Secchi disc depth of Bull Shoals Reservoir, Arkansas, USA. Int J Remote Sens 20:1057–1072

Brazil, ANA. Agência Nacional de Águas. http://www.ana.gov.br/ Brasilia, DF, Brazil

Barbosa CC, Novo EMLM, Pereira Filho W, Melack JM (2006) Metodologia de análise da dinâmica de área e volume inundável: O exemplo da várzea do lago grande de Curuai. RBC. Revistas Brasileiras de Cartografia 58:200-210

Barbosa CCF (2005) Sensoriamento remoto da dinâmica de circulação da água do sistema planície de Curuaí/Rio Amazonas. PhD Thesis, National Institute for Space Research (INPE), São José dos Campos, Brazil

Barbosa CC, Novo EMLM, Pereira Filho W, Carvalho, JC (2004) Planejamento e execução das campanhas de campo na planície de curuai para estudo da dinâmica de circulação da água entre sistemas lóticos, lênticos, e a planície de inundação amazônica. 45p. (INPE-11483-NTC/365). Nota Técnica (Relatório FAPESP) - National Institute for Space Research (INPE), São José dos Campos, Brazil

Barbosa CC, Hess LL, Melack JM, Novo EMLM, (2000) Mapping Amazon Basin Wetlands Through Region Growing Segmentation and Segmented-Based Classification JERS-1 Data". Proceedings of the IX Latin-American Symposium on Remote Sensing held at Universidad Nacional de Lujan. Misiones. Argentina.

Bailey TC, Gatrell AC (1995) Interactive spatial data analysis. Essex, Longman Scientific & Technical

Bins LS, Fonseca LMG, Erthal GJ, Mitsuo II F (1996) Satellite Imagery Segmentation: A region Growing Approach. VIII Simpósio Brasileiro de Sensoriamento Remoto. Salvador-Brazil

Bonnet, M.P., G. Barroux, J.M. Martinez, F. Seyler, P. Moreira-Turcq, G. Cochonneau, J.M. Melack, G. Boaventura, L. Maurice-Bourgoin, J.G. Leon, E. Roux, S. Calmant, P. Kosuth, J.L. Guyot and P. Seyler. Floodplain hydrology in an Amazon floodplain lake (Lago Grande de Curuai).
J. Hydrology, in press.

Braga, C. Z. F. (1999) Sensoriamento remoto aplicado ao estudo da concentração de clorofila-a, transparência e profundidade da água na Lagoa de Araruama, RJ. PhD Thesis, Universidade Federal Fluminense.(INPE-7261-TAE/41)

Burrough PA, McDonnell R.A (1998) Principles of geographical information systems. Oxford. Oxford University Press

Camara G, Souza RCM, Freitas UM, Garrido J (1996) Integrating remote sensing and GIS by object-oriented data modeling. Computers & Graphics, 20:395-403

Costa MPO (1992) Estimativa de clorofila a em água costeira utilizando dados do sensor TM/LANSAT Dissertação (Mestrado em Sensoriamento Remoto) - National Institute for Space Research (INPE), São José dos Campos, Brazil (INPE-6127-TDI/588).

Curran PJ, Novo EMLM (1988) The relationship between suspended sediment concentration and remotely sensed spectral radiance: a review. Journal of Coastal Research, 4:351-368

Dale MRT, Dixon P, Fortin MJ, Legendre P, Myers DE, Rosenberg MS (2002) Conceptual and mathematical relationships among methods for spatial analysis Ecography 25:558–577

Esteves FA. (1998) Fundamentos de limnologia. Interciência, Rio de Janeiro

Gringarten E, Deutsch C (2001) Variogram interpretation and modeling, Math. Geol. 33:507–534

Goovaerts P (1997) Geostatistics for natural resources evaluation. New York, Oxford University Press

Goodin DG, Han L, Fraser RN, Rundquist C, Stebbins WA, Schalles JF (1993) Analysis of Suspended Solids in Water using Remotely Sensed High Resolution Derivative Spectra. Photogramm. Eng. Remote Sensing. 59:505 – 510

Guyot J.L., N. Filizola, and A. Laraque. 2005. Régimes et bilan du flux sédimentaire à Óbidos (Pará, Brésil) de 1995 à 2003. In: Sediment Budgets (D. E. Walling and A. J. Horowitz, eds), IAHS Publ. 291: 347-354.

Hamilton SK, Sippel SJ, Melack JM (2002) Comparison of inundation patterns among major South American floodplains. Journal of Geophysical Research-Atmospheres, 107(D20), 8038, DOI:10.1029/2000JD000306

Hess LL, Melack JM, Novo EMLM, Barbosa CCF, Gastil M (2003) Dual-seasonal mapping of wetland inundation and vegetation for the Central Amazon Basin. Remote Sensing of Environment, 87:404-428

Isaaks EH, Srivastava R M (1989) An Introduction to Applied Geostatistics. New York. Oxford University Press

Junk WJ, Bayley PB, Sparks RE (1989) The flood-pulse concept in river – floodplain systems, in Proceedings of the International Large River Symposium, edited by D. P. Dodge, pp. 110-127, Can. Spec. Publ. Fish. Aquat. Sci. 106, National Research Council of Canada, Ottawa, Ontario

Lewis J, (1996) Turbidity-controlled suspended sediment sampling for runoff-event load estimation. Water Resour. Res., 32:2299-2310

Lewis J, Eads R (1998) Automatic real-time control of suspended sediment sampling based upon high frequency in situ measurements of nephelometric turbidity. In: Proceedings Federal Interagency Workshop: Sediment Technology for the21'st Century. St. Petersburg, FL

Martinez, J.-M., and T. Le Toan. 2007. Mapping of flood dynamics and spatial distribution of vegetation in the Amazon floodplain using multitemporal SAR data. Remote Sens. Environ. 108: 209-223.

Maurice-Bourgoin L., M..P. Bonnet, J.M. Martinez, P. Kosuth, G. Cochonneau, P. Moreira Turcq, J.L. Guyot, P. Vauchel, N. Filizola and P. Seyler. 2007. Temporal dynamics of water and sediment exchanges between the Curuaí floodplain and the Amazon River main stream, Brazil. J. Hydrol. 335: 140-156.

Matheron G (1971) The theory of regionalized variables and its applications. Paris, Les Cahiers du Centre de Morphologie Mathematique de Fontainebleu, 211p.

Morris GL, FAN J (1997) Reservoir sedimentation handbook: design and management of dams, reservoirs, and watersheds for sustainable use. McGraw-Hill, New York.

Mobley CD (1994) The optical properties of water. In: Handbook of Optics (M. Bass. Ed.). McGraw-Hill Book. New York.

Novo EMLM, Barbosa CC, Freitas RM, Shimabukuro YE, Melack JM, Pereira Filho W (2006) Seasonal changes in chlorophyll distributions in Amazon floodplain lakes derived from MODIS images. Limnology 7:153-161 DOI 10.1007/s10201-006-0179-8

Novo EMLM, Hanson JD, Curran PJ (1989) The effect of sediment type on the relationship between reflectance and suspended sediment concentration. International Journal of Remote Sensing, 10:351-368

Petry P, Bayley PB, Markle DF (2003) Relationships between fish assemblages, macrophytes and environmental gradients in the Amazon River floodplain. Journal of Fish Biology. 63:547-579

Rundquist DC, Han L, Schalles JF, Peake JS (1996) Remote measurement of algal chlorophyll in surface waters: the case for the first derivative of reflectance near 690 nm. Photogramm. Eng. Remote Sensing. 62:195:200

Sioli H Hydrochemistry and Geology in the Brazilian Amazon region. Amazoniana. 1:267-277

Nush EA (1980) Comparison of different methods for chlorophyll and phaeopigment determination. Arch. Hydrobiol. Beih. Stuttgart, pp 14-39

Wetzel RG, Likens GE (1991) Limnological Analyses, 2nd Ed., Springer-Verlag, New York

Figure Legends

Fig. 1 – (a) Location of Lago Grande de Curuai. (b) A series of annual hydrographs at LGC. (Data from the Brazilian Water Agency (ANA) (c) Landsat TM image at low water stage (2001/12/12) (d) Landsat TM image at high water stage (2002/07/08)

Fig. 2 – (a)-Direction of flux for each state of the Amazon River/Curuai floodplain system. (b)-Daily mean water level and variation of rates of change estimated from historical (from 1993 to 2002) water level data.

Fig. 3 – Water masses mapped using Landsat TM images for two of the four states of the system and the location of sampling points. (a) rising water stage (state 1). (b) high water stage (state 3).

Fig. 4 – TSS-Turbidity regression model.

Fig. 5 – (a) Thematic clustered map of TSS (state 4). (b) East-West directional lowess for TSS. (c) North-South directional Lowess for TSS.

Fig. 6 – (a) Surface semivariogram for pH (state 2). (b) Empirical semivariograms for pH (state 2).

Fig. 7 – Gray scale images showing the spatio temporal variability of pH, TSS and chlorophyll for four states of LGC floodplain.

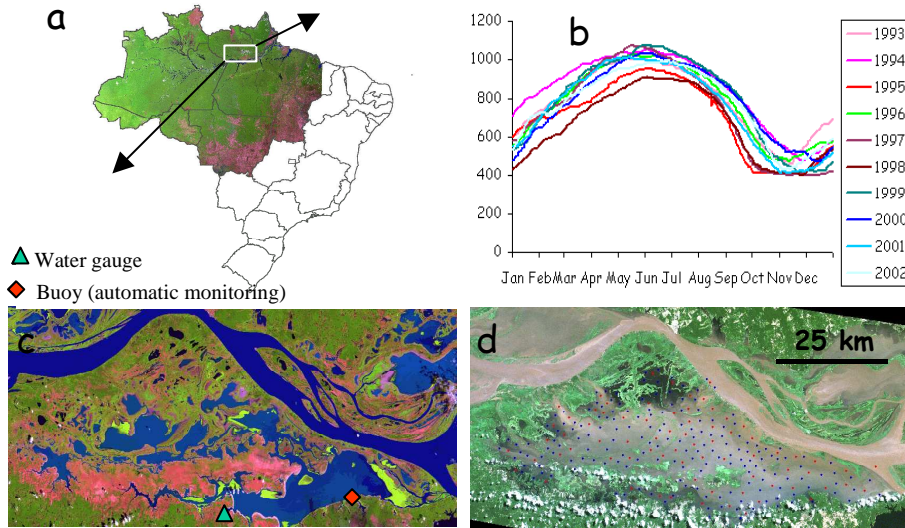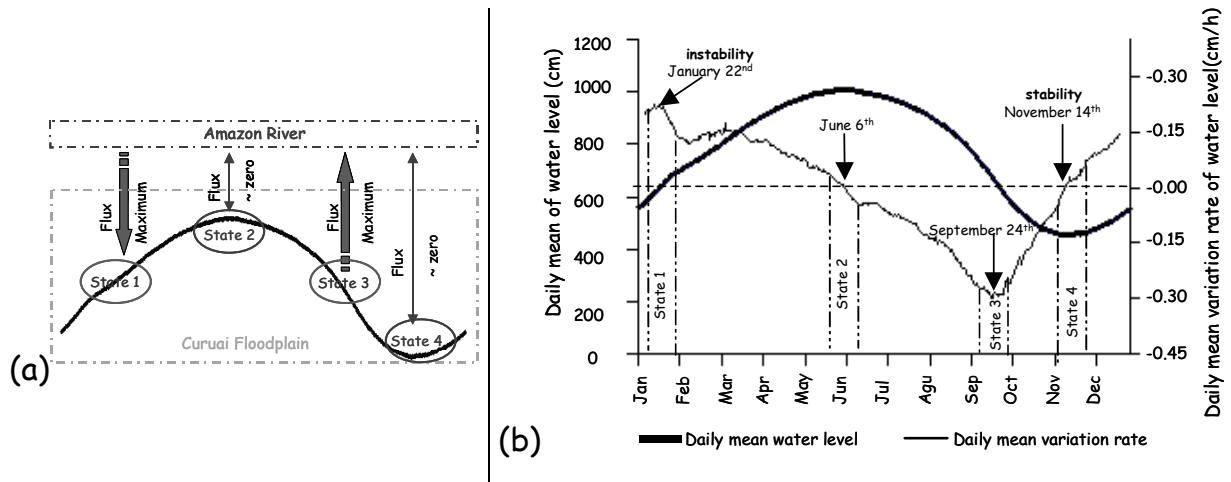**Fig. 8** – (A) Ranges of depth at LGC floodplain for 936 centimeter water level. (B) Wind intensity from 07/2004 to 01/2005
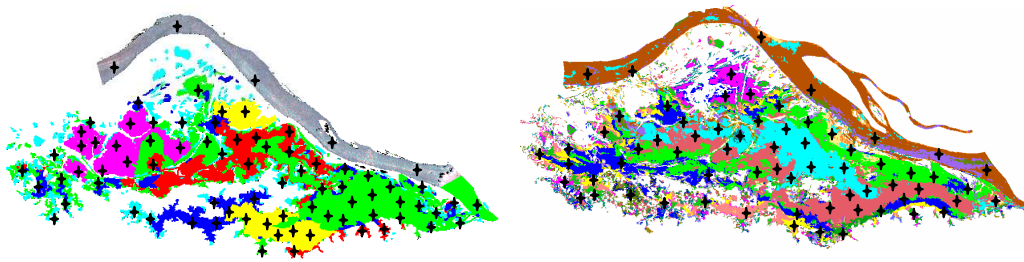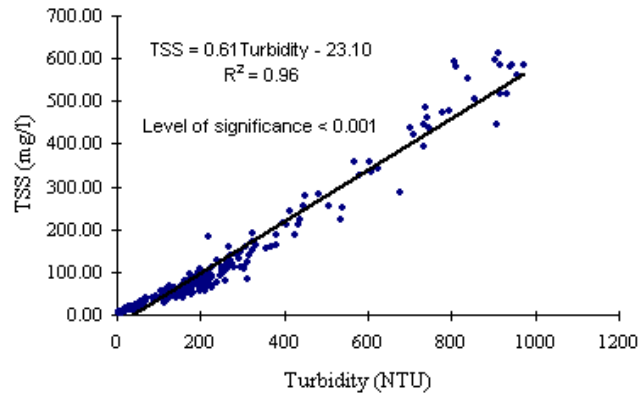
Figure 1.

Figure 2

Figure 3

Figure 4

Figure 5

Figure 6

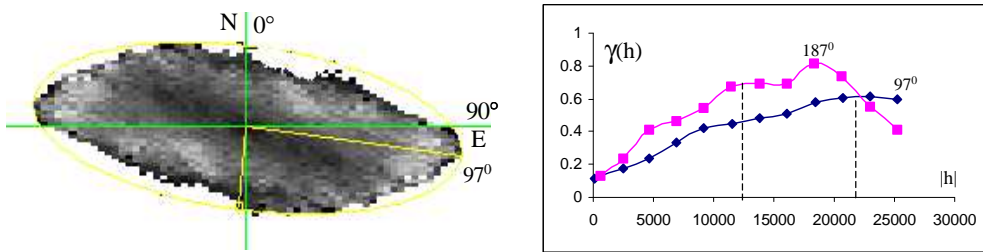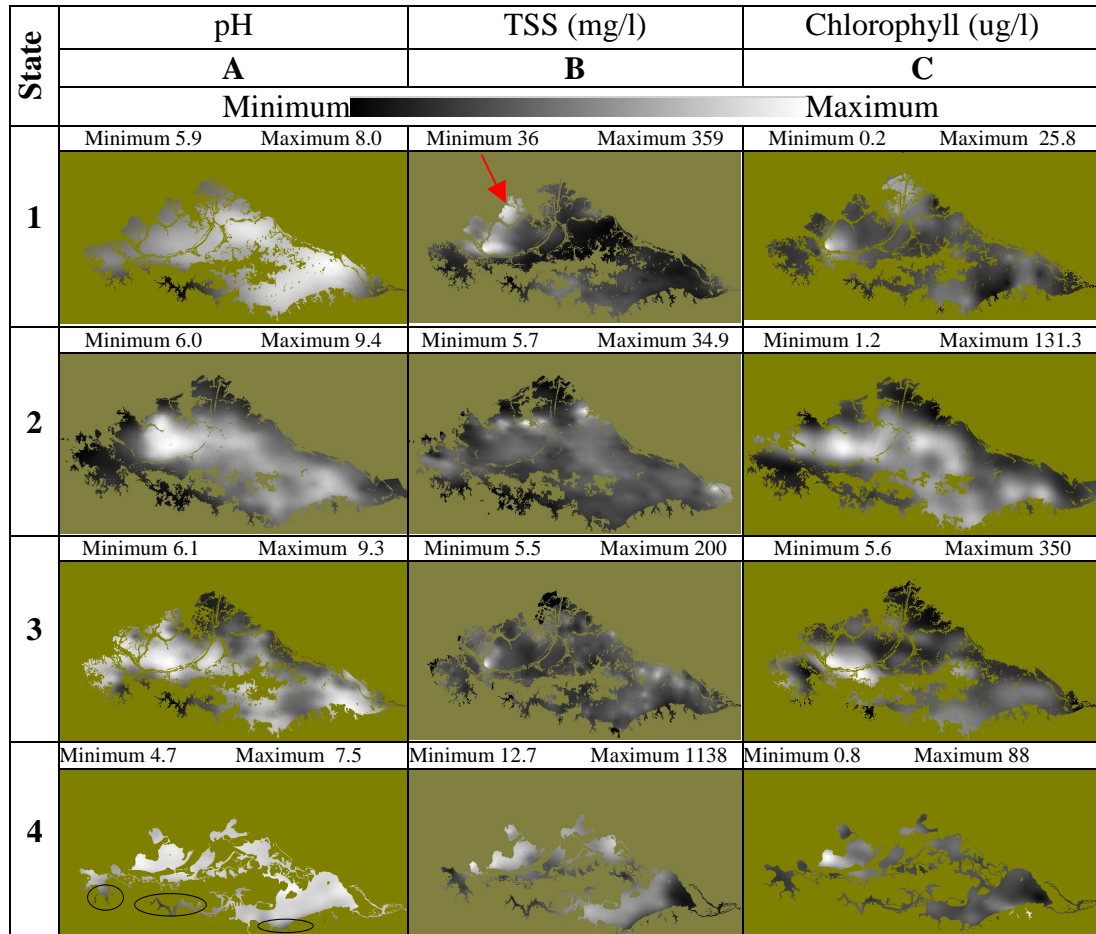| State	pH	TSS (mg/l)	Chlorophyll (ug/l)
	A	**B**	**C**
	Minimum — Maximum		
1	Minimum 5.9 Maximum 8.0	Minimum 36 Maximum 359	Minimum 0.2 Maximum 25.8
2	Minimum 6.0 Maximum 9.4	Minimum 5.7 Maximum 34.9	Minimum 1.2 Maximum 131.3
3	Minimum 6.1 Maximum 9.3	Minimum 5.5 Maximum 200	Minimum 5.6 Maximum 350
4	Minimum 4.7 Maximum 7.5	Minimum 12.7 Maximum 1138	Minimum 0.8 Maximum 88

Figure 7

(A)
(B)
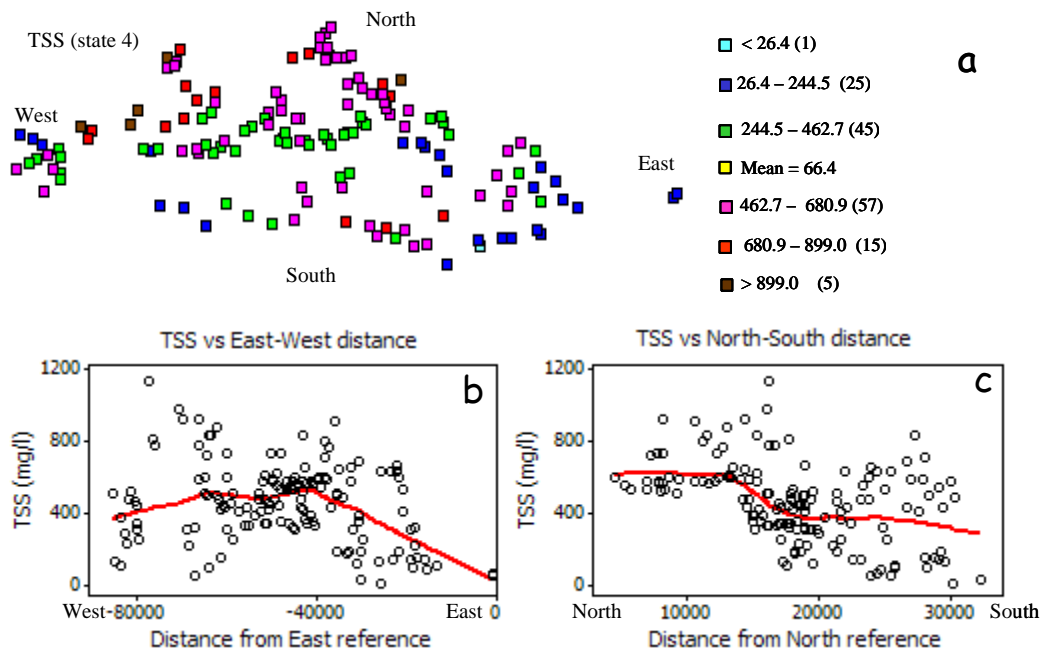
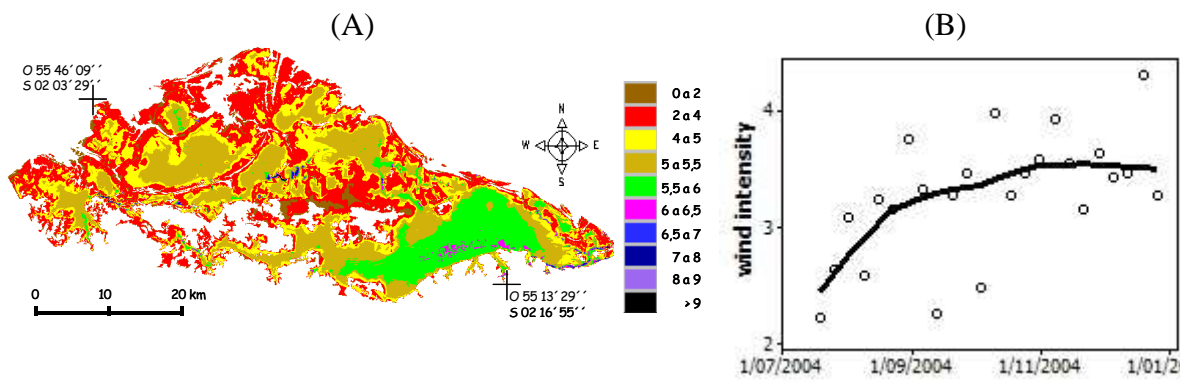Figure 8

Table 1. Maximum and minimum annual water levels from 1993 to 2002.with the month of occurrence in parentheses.

	1993	1994	1995	1996	1997	1998	1999	2000	2001	2002
	Mean (cm)									
Minimum	498(11)	517(11)	415(11)	497(11)	407(11)	412(11)	432(12)	500(12)	421(11)	451(11)
Maximum	1004(5)	1040(5)	945(6)	1018(5)	1062(5)	904(6)	1065(6)	1015(6)	1006(5)	989(6)
Amplitude	506	523	530	521	655	491	633	515	585	538

Table 2. Occurrence period of each state and fieldwork period.

River/floodplain System States	State 1 (rising water)	State 2 (high water)	State 3 (Declining water)	State 4 (low water)
Identified period	01/01 to 02/22	05/18 to 06/30	08/18 to 10/17	11/12 to 12/01
Field campaigns	02/03 to 02/12/04	06/03 to 05/19/04	09/25 to 10/07/03	11/22 to 12/02/03

Table 3 – Statistical description of the selected parameters.

Variable	Month (State)	Minimum value	Maximum value	Mean value (floodplain)	Amazon River
pH	Feb. (1)	5.90	8.00	7.27	6.6
	Jun. (2)	6.01	9.4	7.53	6.6
	Sept. (3)	6.10	9.30	7.72	6.5
	Nov. (4)	4.70	7.50	6.75	6.5
Turbidity (NTU)	Feb. (1)	101.00	569.00	236.78	354
	Jun. (2)	5.00	90.00	29.93	124
	Sept. (3)	12.00	375.00	160.79	62
	Nov. (4)	39.00	1645.00	769	183
TSS (mg/l)	Feb. (1)	36.75	359.42	98.7	161
	Jun. (2)	5.68	34.90	14.51	58
	Sept. (3)	5.46	200	66.13	27.5
	Nov. (4)	12.74	1137.75	462.71	60
Chlorophyll (µg/l)	Feb. (1)	0.21	25.79	8.34	2.3
	Jun. (2)	1.16	131.28	28.85	0.7
	Sept. (3)	5.61	350	68.78	4.15
	Nov. (4)	0.80	87.86	33.4	2

Table 4 – The parameters of the fitted models.

	State	anisotropy Direction	Model: Fitted function	Range (Max./Min.)	Mean error	σ
pH	1	96	Spherical	64000/15700	0.001	0.026
	2	97	Spherical	22700/15150	0.001	0.138
	3	96	Gaussian	15399/11700	0.001	0.003
	4	96	Gaussian	10440/7900	0.013	0.048
TSS	1	100	Spherical	39440/17000	-0.19	866
	2	96	Exponential	9250/4100	0.039	10.0
	3	105	Exponential	5700/5700	0.57	460
	4	96	Gaussian	8865/6825	-5.8	105
Chlorophyll	1	96	Gaussian	5300/5300	-0.05	3.9
	2	96	Gaussian	10600/8600	1.0	11.6
	3	96	Gaussian	15000/7500	-0.78	60
	4	106	Gaussian	7200/5320	0.80	13